

# Chiral Electron-Hole Pairing as the Origin of Anomalous Quasiparticle Dispersions in Unconventional Superconductors

Wanpeng Tan\*

*Department of Physics and Astronomy,  
University of Notre Dame, Notre Dame, Indiana 46556, USA*

(Dated: February 27, 2026)

The microscopic pairing mechanism in unconventional superconductors remains elusive, largely because the extreme flatness of the superconducting band often obscures key energy-momentum dispersion features observed in angle-resolved photoemission spectroscopy. In this work, we re-examine high-resolution dispersion data from cuprates (Bi2212 and Bi2201) and iron-based superconductors (monolayer FeSe) to test the predictions of a newly proposed chiral electron-hole (CEH) pairing mechanism. Unlike Cooper pairs in BCS-like theories that form a single quasiparticle band with a smooth back-bending dispersion, CEH pairs exhibit a distinct two-band structure in quasiparticle dispersion with sharp cusps at the back-bending points. Our analysis identifies clear empirical signatures of these CEH-predicted features, concluding that quasiparticle dispersions in these strongly correlated materials deviate significantly from BCS-like behavior. Further comprehensive and targeted experimental strategies are proposed to definitively resolve the subtle dispersion features and rigorously test the CEH model for unconventional superconductivity.

## I. INTRODUCTION

Angle-resolved photoemission spectroscopy (ARPES) [1] has emerged as an indispensable technique in the study of unconventional superconductors. Notably, it has been instrumental in determining superconducting gap symmetries, such as the discovery of the  $d_{x^2-y^2}$  d-wave gap symmetry in cuprates [2]. Moreover, ARPES serves as a powerful tool for elucidating the band structures of superconducting materials, particularly by revealing the energy-momentum dispersion of the quasiparticles responsible for superconductivity.

The two primary classes of high- $T_c$  superconductors — cuprate [3] and iron-based (FeSC) [4] materials — exhibit behaviors that diverge fundamentally from those of conventional superconductors that are well described by Bardeen-Cooper-Schrieffer (BCS) theory [5]. Both cuprates and FeSCs are strongly correlated electronic systems proximate to their antiferromagnetic (AFM) parent compounds, and many of their properties evade explanation within traditional BCS or BCS-like frameworks. Despite this, a 2003 ARPES study reported evidence of BCS-like quasiparticle dispersion in nearly optimally doped Bi-2223 ( $T_c = 108$  K) [6]. A crucial caveat to this claim, however, is that at temperatures  $T \ll T_c$ , the associated band for such nearly perfect superconductors is exceedingly flat relative to the instrumental resolution of ARPES, rendering it incapable of definitively distinguishing between different types of dispersion relations.

---

\* wtan@nd.edu

25 In this work, we utilize more recently published high-resolution ARPES data [7–11] to  
 26 demonstrate that the quasiparticle dispersions in cuprates and FeSCs deviate significantly  
 27 from BCS-like behavior. Instead, the observed dispersion features align closely with the  
 28 predictions of a recently proposed pairing mechanism driven by chiral electron-hole (CEH)  
 29 condensation [12]. The CEH framework intrinsically necessitates strongly correlated AFM  
 30 materials for non-BCS superconductivity. Furthermore, it accounts for numerous puzzling  
 31 properties observed in cuprates and FeSCs, including the pseudogap phenomenon, the ab-  
 32 sence of gap closure at  $T_c$ , unexpectedly large  $\Delta_0/T_c$  ratios, and a non-zero  $\gamma(0)$  term and  
 33 a quadratic temperature dependence in the specific heat ratio  $C/T$  as  $T \rightarrow 0$  in d-wave  
 34 cuprates [12].

35 In the subsequent sections, we first outline the CEH pairing mechanism and analyze  
 36 its unique predicted dispersion features, specifically the emergence of two-band structures  
 37 and cusps at the back-bending points. We then present and discuss detailed comparisons  
 38 with recent high-resolution ARPES measurements. Ultimately, these comparisons provide  
 39 compelling evidence for further systematic investigations to verify the theoretical predictions  
 40 of the CEH model.

## 41 II. CHIRAL ELECTRON-HOLE (CEH) PAIRING

42 To introduce the CEH pairing mechanism within a mean-field framework, we begin with  
 43 a four-fermion interacting Hamiltonian,

$$H = \sum_{\mathbf{k}\sigma} \xi_{\mathbf{k}} c_{\mathbf{k}\sigma}^\dagger c_{\mathbf{k}\sigma} - V \sum_{\mathbf{k}\mathbf{k}'} c_{\mathbf{k}L}^\dagger c_{-\mathbf{k}R} c_{-\mathbf{k}'R}^\dagger c_{\mathbf{k}'L} \quad (1)$$

44 where  $\xi_{\mathbf{k}}$  denotes the single-particle energy relative to the Fermi surface, assuming perfect  
 45 particle-hole and chiral symmetries. Note that left (L) and right (R) chiralities are used  
 46 here to replace the conventional up and down spin notation.

47 Traditional BCS theory postulates that a system becomes superconducting due to the  
 48 condensation of electron-electron Cooper pairs  $\langle c_{\mathbf{k}L} c_{-\mathbf{k}R} \rangle$ . In the new CEH model, how-  
 49 ever, superconductivity arises from the condensation of chiral electron-hole pairs, with the  
 50 corresponding order parameter  $\Delta$  defined as,

$$\Delta = V \sum_{\mathbf{k}} \langle c_{\mathbf{k}L}^\dagger c_{-\mathbf{k}R} \rangle, \quad \Delta^* = V \sum_{\mathbf{k}} \langle c_{-\mathbf{k}R}^\dagger c_{\mathbf{k}L} \rangle. \quad (2)$$

51 This leads to the following Bogoliubov-de Gennes (BdG) Hamiltonian,

$$H = \sum_{\mathbf{k}} (c_{\mathbf{k}L}^\dagger, c_{-\mathbf{k}R}^\dagger) \begin{pmatrix} \xi_{\mathbf{k}} & -\Delta^* \\ -\Delta & \xi_{\mathbf{k}} \end{pmatrix} \begin{pmatrix} c_{\mathbf{k}L} \\ c_{-\mathbf{k}R} \end{pmatrix} + \frac{|\Delta|^2}{V}. \quad (3)$$

52 which can be diagonalized via the Bogoliubov transformation. The resulting eigen-energies  
 53 of the Bogoliubov CEH quasiparticles are

$$E_{\mathbf{k}}^\pm = \xi_{\mathbf{k}} \pm |\Delta|, \quad (4)$$

54 which contrasts sharply with the standard BCS-like dispersion relation,  $E_{\mathbf{k}}^\pm = \pm \sqrt{\xi_{\mathbf{k}}^2 + |\Delta|^2}$ .  
 55 This striking difference in energy-momentum dispersion constitutes the primary focus of this  
 56 paper.

57 It is worth noting that both the BCS and CEH mechanisms for superconductivity bear  
 58 conceptual similarities to neutrino or neutron-mirror neutron oscillations [13, 14], origi-  
 59 nating from the unitary mixing between misaligned interaction and energy eigenstates. A  
 60 particularly intriguing reciprocal relationship exists between the two models: the energy  
 61 eigenstates of Cooper pairs are a superposition of two CEH-pair-like particles (i.e., mixing  
 62 of chirally opposite electrons and holes), whereas the energy eigenstates of CEH pairs are a  
 63 superposition or mixing of two Cooper-pair-like electrons or holes.

64 A fundamental distinction between the two models is that BCS quasiparticles are char-  
 65 acterized by a single energy branch,  $\sqrt{\xi_{\mathbf{k}}^2 + |\Delta|^2}$ , whereas CEH quasiparticles possess two  
 66 distinct energy branches,  $|\Delta| \pm |\xi_{\mathbf{k}}|$ , resulting in a two-band structure and cusps at the  
 67 back-bending points. In addition, the Bogoliubov mixing angle in BCS theory, defined as  
 68  $\theta_{\mathbf{k}}^{\text{BCS}} = \arctan |v_{\mathbf{k}}/u_{\mathbf{k}}|$ , varies greatly between 0 and  $\pi/2$  satisfying  $\tan(2\theta_{\mathbf{k}}) = -|\Delta|/\xi_{\mathbf{k}}$ .  
 69 In contrast, the CEH mixing angle,  $\theta_{\mathbf{k}}^{\text{CEH}}$ , remains constant at  $\pi/4$  as  $|u| = |v| = 1/\sqrt{2}$   
 70 assuming perfect chiral symmetry with  $\xi_{\mathbf{k}L} = \xi_{\mathbf{k}R}$ .

71 Depending on the orbital pairing symmetry, the CEH mechanism can yield an angular-  
 72 dependent superconducting energy gap,  $\Delta_{\mathbf{k}} \equiv |\Delta_{\mathbf{k}}| = \Delta\gamma_{\mathbf{k}}$ . For the  $d_{x^2-y^2}$  d-wave gap  
 73 symmetry typical of cuprate superconductors, the symmetry factor  $\gamma_{\mathbf{k}} = |\cos k_x a - \cos k_y b|/2$   
 74 can be approximated as  $\cos(2\varphi)$ . This substitution leads to the following d-wave CEH gap  
 75 equation [12],

$$\Delta(T) = \frac{8\lambda T}{\pi} \int_0^{\pi/4} d\varphi \tanh^{-1} \left( \tanh\left(\frac{\Delta(T) \cos(2\varphi)}{2T}\right) \tanh\left(\frac{\omega^*}{2T}\right) \right) \quad (5)$$

76 where the single-particle energy is integrated over the flat band (defined by  $\pm\omega^*$  around  
 77 the fermi surface), and  $\lambda = V\rho_F$  represents the dimensionless coupling constant. Strikingly,  
 78 this d-wave gap equation requires  $\lambda > \pi/2$  (or  $\lambda > 1$  for s-wave), indicating that the CEH  
 79 mechanism is intrinsically suited for strongly correlated electron systems [12].

80 In the presence of chiral asymmetry, the modified dispersion and the Bogoliubov mixing  
 81 angle can be expressed as,

$$E_{\mathbf{k}}^{\pm} = \frac{\xi_{\mathbf{k}L} + \xi_{\mathbf{k}R}}{2} \pm \sqrt{\Delta_{\mathbf{k}}^2 + \left(\frac{\xi_{\mathbf{k}L} - \xi_{\mathbf{k}R}}{2}\right)^2}, \quad (6)$$

$$\tan \theta_{\mathbf{k}}^{\text{CEH}} = \sqrt{1 + \left(\frac{\xi_{\mathbf{k}L} - \xi_{\mathbf{k}R}}{\Delta_{\mathbf{k}}}\right)^2} - \frac{\xi_{\mathbf{k}L} - \xi_{\mathbf{k}R}}{\Delta_{\mathbf{k}}}. \quad (7)$$

82 It is important to emphasize that the CEH pairing mechanism favors antiferromagnetism,  
 83 and strong electronic correlations inherently lead to its non-local behavior. While it is well  
 84 established that the superconducting gap decreases as temperature increases, the flat-band  
 85 width,  $\omega^*$ , may also exhibit temperature dependence, becoming flatter at lower temperatures  
 86 as illustrated in the schematic diagram of Fig. 1. Crucially, the onset of superconductivity  
 87 requires [12],

$$\omega^*(T) \leq \Delta(T), \quad (8)$$

88 meaning that the band ( $\pm\omega^*$ ) in which the CEH quasiparticles form must be sufficiently flat  
 89 so as not to exceed the superconducting gap  $\Delta$ . No analogous requirement exists within BCS  
 90 theory. Consequently, in the CEH framework, the critical temperature  $T_c$  is defined by the  
 91 condition  $\omega^*(T_c) = \Delta(T_c)$ , whereas the gap-closing temperature  $T_0$  is defined by  $\Delta(T_0) = 0$ .

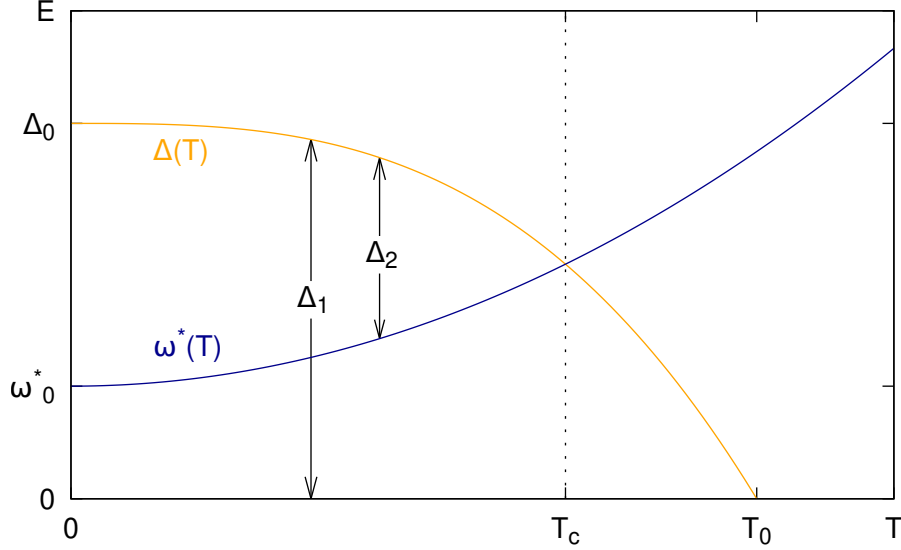


FIG. 1. Schematic diagram illustrating the temperature dependence of the superconducting gap  $\Delta$  and the flat-band width  $\omega^*$  with the two-gap structure of  $\Delta_1 = \Delta$  and  $\Delta_2 = \Delta - \omega^*$ . The critical temperature,  $T_c$ , is defined as the point where the band width equals the superconducting gap or  $\Delta_2 = 0$ , while  $T_0$  denotes the gap-closing temperature ( $\Delta_1 = 0$ ).

92

### III. ENERGY-MOMENTUM DISPERSION

93 An optimal strategy for distinguishing the CEH quasiparticle dispersion from other BCS-  
 94 like models involves conducting high-resolution ARPES measurements along the Brillouin  
 95 zone (BZ) boundary, traversing an antinode and two adjacent Fermi surfaces in cuprates.  
 96 In this momentum region, the unique spectral features predicted by the CEH model become  
 97 pronounced. Specifically, because the two Fermi surfaces are in close proximity, the d-wave  
 98 superconducting gap is near its maximum and approximately constant, allowing the single-  
 99 particle dispersion to be well modeled by a parabola. Consequently, the observation of cusps  
 100 at the back-bending points, alongside a distinct two-band structure, would provide definitive  
 101 evidence for the CEH mechanism.

102 A schematic representation of the first Brillouin zone for the 2D  $\text{CuO}_2$  layer is provided  
 103 in the right-panel inset of Fig. 2. The thick red bar along the BZ boundary, which crosses  
 104 the  $(0, \pi)$  antinode, indicates the momentum trajectory along which the energy-momentum  
 105 dispersion is analyzed here. This cut lies also within the AFM zone and yields a nearly  
 106 constant d-wave superconducting gap, characterized by the symmetry factor  $\gamma_{\mathbf{k}} = (\cos k_{\parallel} a +$   
 107  $1)/2 \simeq 1$  (e.g., lattice constants  $a = b = 5.4\text{\AA}$  for Bi-2212 superconductors).

108 Figure 2 illustrates the normal-state and quasiparticle energy bands relative to the Fermi  
 109 level as a function of the parallel momentum along the cut and the corresponding d-wave  
 110 symmetry factor  $\gamma_{\mathbf{k}}$ . On the left panel, the solid and dashed parabolas represent the normal-  
 111 state dispersion for the electron and hole branches, respectively, residing within a relatively  
 112 flat band and assuming perfect particle-hole symmetry. In the superconducting state, de-  
 113 picted on the right panel, a gap opens, yielding a single quasiparticle band in each branch  
 114 according to a BCS-like theory (indicated by the blue lines).

115 In contrast, the CEH mechanism generates two distinct quasiparticle bands within each

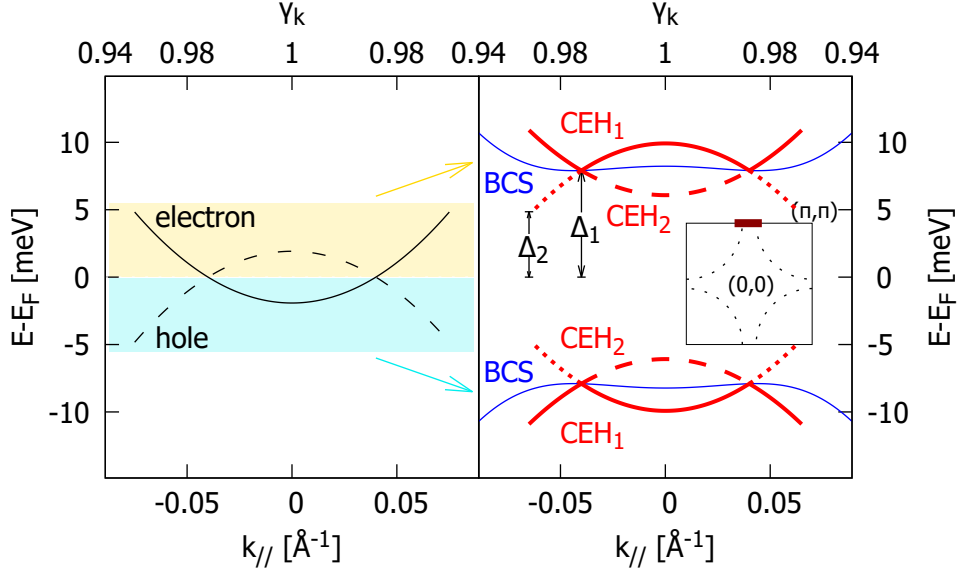


FIG. 2. Schematic comparison of the energy-momentum dispersions transitioning from the normal state (left panel) to the gapped superconducting phase (right panel) for both the CEH and BCS-like models.  $\gamma_{\mathbf{k}}$  is calculated for Bi-2212. The thick red bar traversing the  $(0, \pi)$  antinode in the BZ inset indicates the momentum cut corresponding to the displayed dispersions.

116 branch (denoted by solid red lines for band 1, and dashed/dotted red lines for band 2). In  
 117 the superconducting phase, the primary CEH quasiparticle dispersion (band 1, representing  
 118 the more energetic quasiparticles) is governed by,

$$E - E_F = \pm(|\Delta_{\mathbf{k}}| + |\xi_{\mathbf{k}}|) \quad (9)$$

119 which shows distinct, sharp cusps at the back-bending points, fundamentally differing from  
 120 the smooth transitions characteristic of BCS-like dispersions. Most remarkably, unlike the  
 121 BCS framework where quasiparticles share one single dispersion, CEH quasiparticles split  
 122 into two distinct energy branches. The less energetic quasiparticles form a secondary band  
 123 (band 2) governed by,

$$E - E_F = \pm(|\Delta_{\mathbf{k}}| - |\xi_{\mathbf{k}}|). \quad (10)$$

124 Consequently, as illustrated in Fig. 2, two corresponding energy gaps ( $\Delta_1$  and  $\Delta_2$ ) are  
 125 associated with these distinct quasiparticle bands.

126 This two-gap feature, inherent to the CEH model and possibly first observed in La-  
 127 Bi2201 in 2008 [15], naturally accounts for the pseudogap phenomenon, particularly given  
 128 that  $\Delta_1 = \Delta$  does not vanish above  $T_c$ . As such, macroscopic superconductivity emerges  
 129 only when  $\Delta_2 = \Delta - \omega^* > 0$ , a criterion identical to the condition established in Eq. 8. It also  
 130 clarifies why relatively flat bands (characterized by smaller  $\omega^*$ ) are a necessary precondition  
 131 for CEH-driven superconductivity.

132 While the primary band (band 1) has been observed in many prior studies, explicit evi-  
 133 dence of cusps at the back-bending points has remained elusive. This is largely attributable  
 134 to limitations in ARPES resolution relative to the extreme flatness of these bands. Empiri-  
 135 cal evidence for band 2 (the dashed and dotted red lines in Fig. 2) is even more scarce  
 136 within the existing literature. In the following analysis, we present renewed evidence for  
 137 both features utilizing recently published, high-resolution ARPES data.

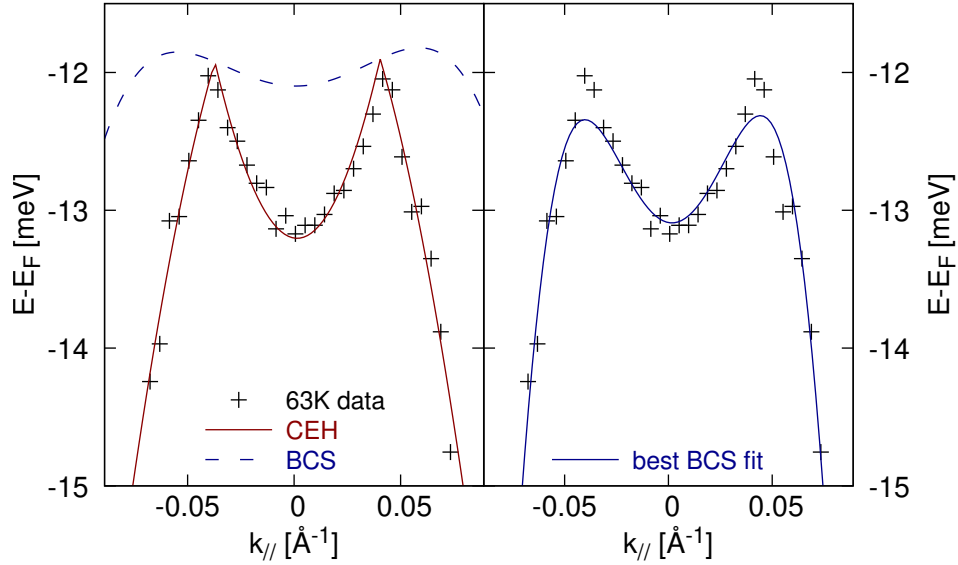


FIG. 3. Quasiparticle dispersion at  $T = 63$  K (just below  $T_c = 66$  K) for the Bi-2212 sample OD66, utilizing data from Ref. [7]. Left: The CEH dispersion (solid red curve) yields an excellent fit to the experimental data; the corresponding BCS-like dispersion (dashed blue curve) is shown for comparison. Right: The best BCS-like fit (solid blue curve) fails to reproduce the observed cusps at the back-bending points.

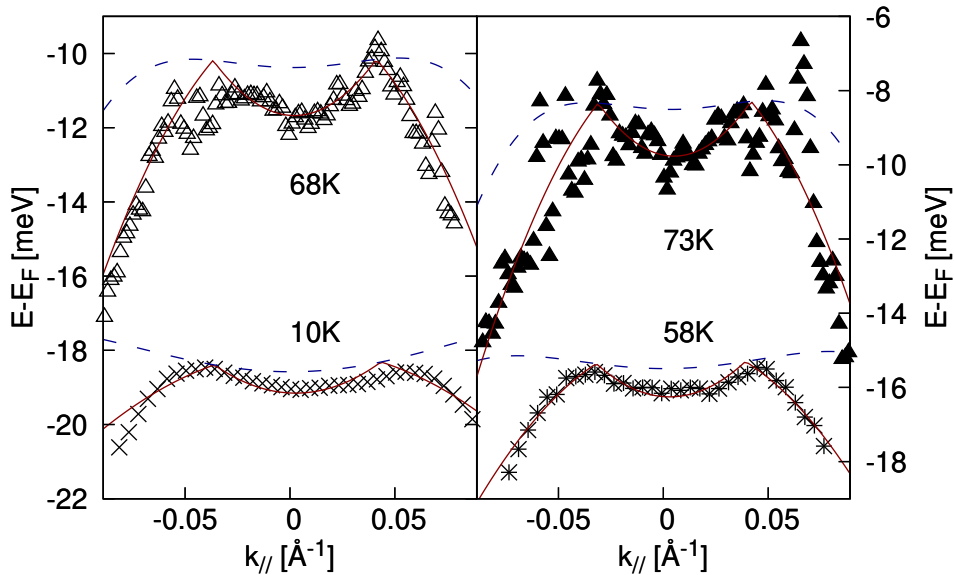


FIG. 4. Quasiparticle dispersions at other temperatures for the Bi-2212 sample OD66, with data from Ref. [7]. The CEH dispersions (solid red curves) fit the data well, particularly in reproducing the back-bending cusps, with the notable exception of the 10 K measurement. BCS-like dispersions (dashed blue curves), calculated using the fitted normal-state dispersion, are provided for comparison.

138 Compelling evidence for the presence of cusps in band 1 is presented in Fig. 3, which  
 139 displays the dispersion measured near  $T_c$  for the Bi-2212 sample OD66 [7]. This data is fitted  
 140 under the assumption of a simple parabolic normal-state dispersion, implying robust chiral  
 141 and particle-hole symmetries. The CEH dispersion (solid red curve, left panel) demonstrates  
 142 excellent agreement with the experimental data. Conversely, the best BCS-like fit (solid blue  
 143 curve, right panel) fails to reproduce the cusps at the back-bending points and it artificially  
 144 requires a significantly steeper normal-state dispersion, comparable to the measurements  
 145 taken at  $T = 145$  K, which is at odds with the evidence discussed below.

146 Dispersions and corresponding fits at various other temperatures for the same OD66  
 147 sample are detailed in Fig. 4. Because the superconducting gap is nearly constant in this  
 148 momentum region, the extended “wings” beyond the back-bending points predominantly  
 149 dictate the shape of the underlying single-particle (hole) parabolic dispersion that should  
 150 agree with its electron counterpart determined by the quasiparticle dispersion in between  
 151 the back-bending points assuming particle-hole symmetry. Notably, the band flattens at  
 152 lower temperatures, indicative of an increasing effective mass as the system cools.

153 The measurement at  $T = 63$  K provides the clearest resolution of the cusp feature by  
 154 striking an optimal balance between minimized experimental uncertainty and a band that  
 155 is not yet excessively flat compared to lower-temperature data (as shown in Fig. S1). Con-  
 156 sequently, fits at other temperatures are comparatively less definitive. Specifically, the fit  
 157 at  $T = 10$  K is limited by the extreme flatness of the band at such a low temperature. The  
 158 extracted normal-state dispersions at these temperatures with fitting parameters summa-  
 159 rized in Table I are plotted in Fig. S2, consistently demonstrating the progressive flattening  
 160 of the band as temperature decreases. This temperature-dependent flattening is indepen-  
 161 dently corroborated by the findings in Figs. 3i–j and S13a–b of Ref. [7], which show that  
 162 the normal-state dispersion at 86 K (where the gap is nearly closed) is substantially flatter  
 163 than the one at 145 K.

164 Further evidence of cusps in band 1 is provided in Fig. 5 with fitting parameters sum-  
 165 marized in Table II, displaying data for the Bi-2212 sample OD49 [7]. Here, the dispersions  
 166 exhibit even more pronounced cusps due to the reduced flatness of the superconducting  
 167 band. However, this sample also presents stronger chiral and particle-hole asymmetries.  
 168 To better fit the quasiparticle dispersion, an averaged experimental normal-state dispersion  
 169 (black stars in the right panel of Fig. 5), measured at higher temperatures, is scaled down,  
 170 using distinct scaling factors for the electron and hole branches to account for the band  
 171 flatness at lower temperatures. Such scaling is demonstrated for the 45-K fit on the right  
 172 panel. The discrepancies observed at the right back-bending points likely originate from  
 173 misaligned single-particle dispersions or other distortions near the Fermi level (unaccounted  
 174 in the fitting), which is also visible, albeit to a much lesser extent, in the OD66 data (Fig.  
 175 S1).

176 Arguably the most comprehensive evidence capturing the features of both CEH bands  
 177 is found in the ARPES data (Fig. 6) for superconducting monolayer FeSe films grown on  
 178 SrTiO<sub>3</sub> [8]. These spectra were acquired along a momentum cut through an electron pocket  
 179 centered at the M-point, which is analogous to the antinodal cut analyzed in the cuprates.  
 180 CEH band 1 traced by the solid red curve and band 2 indicated by the dashed red line in  
 181 Fig. 6c, originally conflated as labels A' and B in the source reference, are both clearly  
 182 resolved. Because these bands are situated deeply ( $\sim 100$  meV below the Fermi surface)  
 183 and lack the extreme flatness seen in cuprates, the signature CEH features are starkly  
 184 visible. Although the band closer to the Fermi surface (band A, marked by the blue line)

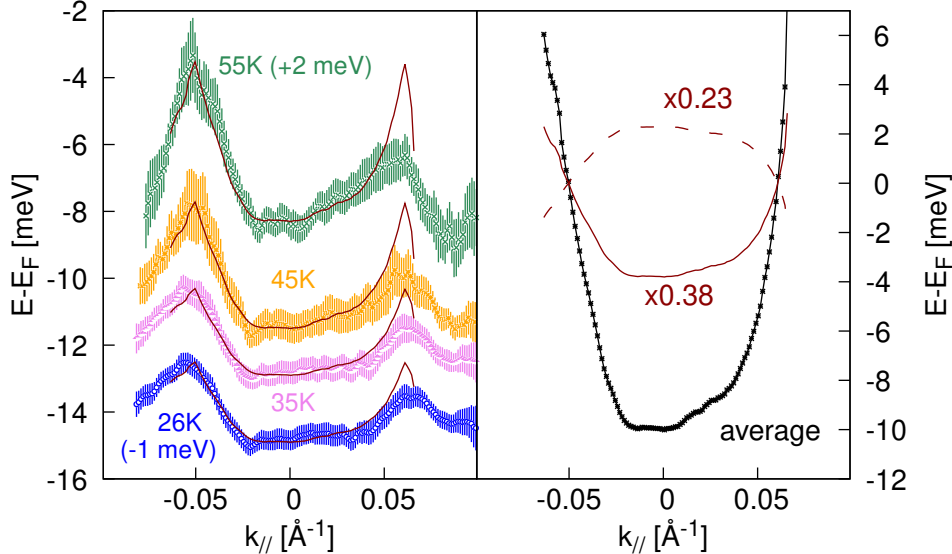


FIG. 5. Left: Dispersion data at varied temperatures for the Bi-2212 sample OD49 from Ref. [7], overlaid with CEH fits (red curves). Select datasets are offset as labeled for clarity. Right: Average normal-state dispersion data (black stars) acquired between 65 K and 95 K (from Fig. S14b of Ref. [7]), and its scaling demonstration for a representative CEH fit at  $T = 45$  K, which uses the solid and dashed red curves with band scaling factors of 0.38 and 0.23 for the electron and hole normal states, respectively.

185 is the one primarily responsible for superconductivity in this system, the authors of Ref.  
 186 [8] convincingly demonstrated that these deeper CEH bands are exclusively associated with  
 187 superconducting monolayer FeSe and are entirely absent in non-superconducting multilayer  
 188 samples.

189 These quasiparticle dispersion relations in FeSe are further illustrated by the waterfall  
 190 plot of energy distribution curves (EDCs) in Fig. 6a [8]. In this representation, the central  
 191 segment of CEH band 2 (corresponding to the dashed red lines in Figs. 2 and 6c) manifests  
 192 clearly as a structural shoulder next to CEH band 1. Intriguingly, similar shoulder features  
 193 have been reported in the literature for other superconductors. For instance, the data for  
 194 Bi-2201 shown in Fig. S3 [9] explicitly display this shoulder feature characteristic of band  
 195 2, and simultaneously exhibit indications of cusps in band 1. The shoulder feature becomes  
 196 more pronounced at lower temperatures, as illustrated in similar plots in Figs. 2 and 4 of  
 197 Ref. [9], Fig. 1 of Ref. [10], and Fig. 4 of Ref. [11].

198 Despite these observations, the extended “wings” of band 2 (represented by the dotted  
 199 red lines in Fig. 2) seem to be much less discernible in published data. A weak spectral  
 200 feature (labeled as band C in Fig. 6b) may offer tentative evidence of their existence. More  
 201 inspiringly, the temperature-dependent ARPES spectra and EDC plots from Ref. [7] (Figs.  
 202 3e-h and S13c-f therein) reveal ridges crossing the Fermi surfaces that start to develop near  
 203 or above  $T_c$ . These ridges could plausibly represent the emerging wings of band 2. Future  
 204 investigations, particularly those leveraging advanced ARPES image-processing techniques,  
 205 are essential to definitively isolate and clarify this subtle spectral feature.

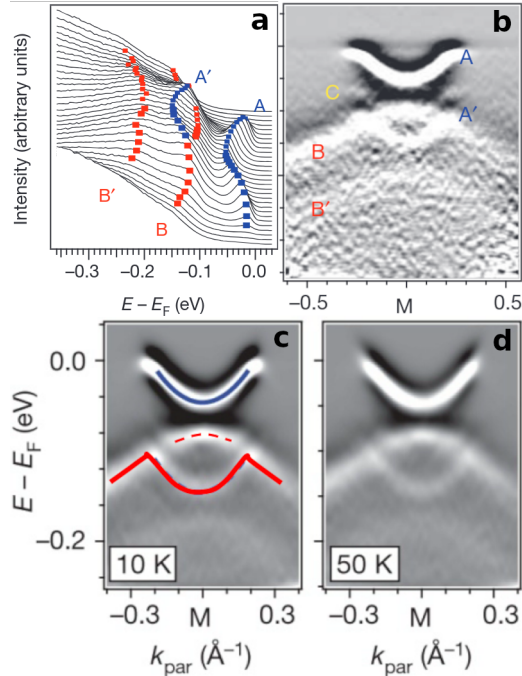


FIG. 6. Quasiparticle band dispersions intersecting an electron pocket centered at the M-point for monolayer FeSe on SrTiO<sub>3</sub> [8]. (a) EDCs presented as a waterfall plot. (b) Second-derivative intensity plot at 16 K, with bands labeled corresponding to (a). (c,d) Intensity plots at different temperatures; the solid red curve traces CEH band 1, while the dashed red line indicates CEH band 2. Adapted from Figs. 1 and 3 of Ref. [8].

206

#### IV. CONCLUSIONS AND OUTLOOK

207 We have re-examined previously published data to present compelling evidence for the  
 208 unique two-band structure and cusp features in quasiparticle dispersion, as predicted by the  
 209 recently proposed chiral electron-hole pairing mechanism for non-BCS superconductivity. To  
 210 further validate these findings, future high-precision ARPES studies are essential, particu-  
 211 larly those focused on the antinodal cut along the BZ boundary in cuprates and the M-point  
 212 cut in FeSCs. Comprehensive and systematic measurements of these materials across a  
 213 wider range of doping levels and temperatures are highly encouraged. Specifically, to make  
 214 signatures like the back-bending cusps more pronounced, experimental efforts should target  
 215 underdoped or sub-optimal superconductors near  $T_c$ , where the associated superconducting  
 216 bands exhibit reduced flatness. Finally, to better visualize and extract these complex quasi-  
 217 particle dispersions, analyses must move beyond the simple fitting of EDC maxima. The  
 218 application of advanced techniques such as the second-derivative approach, the curvature  
 219 method [16], and possibly machine learning algorithms and emerging AI technology, will be  
 220 critical for definitively resolving these subtle spectral features in future research.

221

#### ACKNOWLEDGMENTS

222 This work is supported in part by the faculty research support program at the University  
 223 of Notre Dame. We extend our gratitude to Sudi Chen for valuable early discussions, and

224 to both Sudi Chen and Yu He for generously providing the tabulated data used in their  
 225 publication [7].

226

### SUPPLEMENTARY MATERIALS

227 This appendix provides additional experimental dispersion data and normal-state deriva-  
 228 tions used to support the fits in the main text.

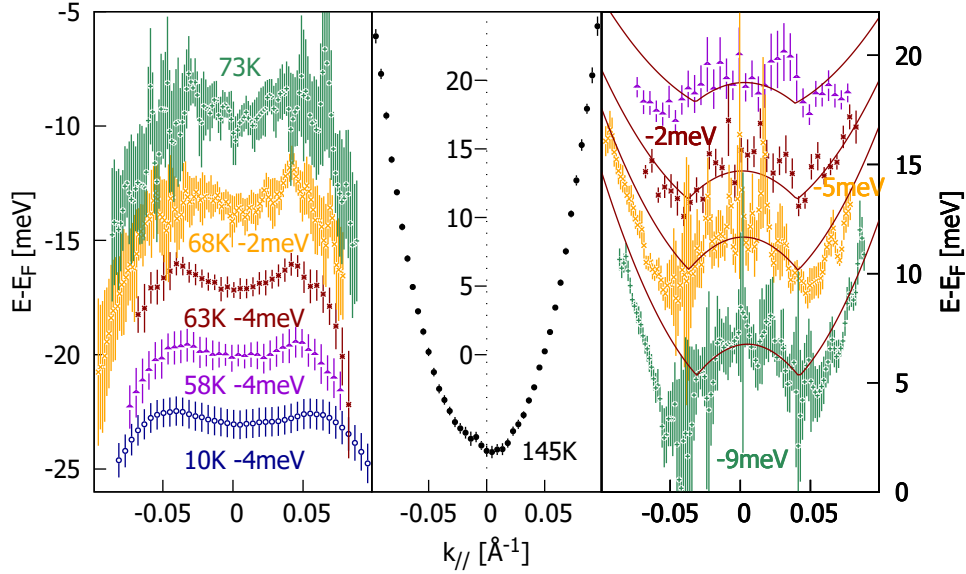


FIG. S1. Experimental dispersions at varied temperatures for the Bi-2212 sample OD66 [7], obtained by fitting the maxima of Fermi-function-divided EDCs, as provided by the original authors. Data for 68 K and 73 K are taken from Fig. S16a,d of Ref. [7], while the remaining data are sourced from Figs. 3k and S15 of the same reference. Select dispersion curves are vertically offset by a few meV for clarity, as labeled. The red curves in the right panel are generated by applying the CEH fitting results from the lower branch to the upper branch, with slight shifts incorporated to account for particle-hole asymmetry.

TABLE I. CEH fitting parameters for Figs. 3-4.

T [K]	normal-state parabola [meV]	$\Delta$ [meV]
10	$371.27(k_{\parallel} + 0.03609)(k_{\parallel} - 0.04341)$	18.57
58	$618.15(k_{\parallel} + 0.03198)(k_{\parallel} - 0.03915)$	15.47
63	$771.14(k_{\parallel} + 0.03720)(k_{\parallel} - 0.04039)$	12.04
68	$916.06(k_{\parallel} + 0.03667)(k_{\parallel} - 0.04116)$	10.29
73	$1029.61(k_{\parallel} + 0.03108)(k_{\parallel} - 0.04188)$	8.40

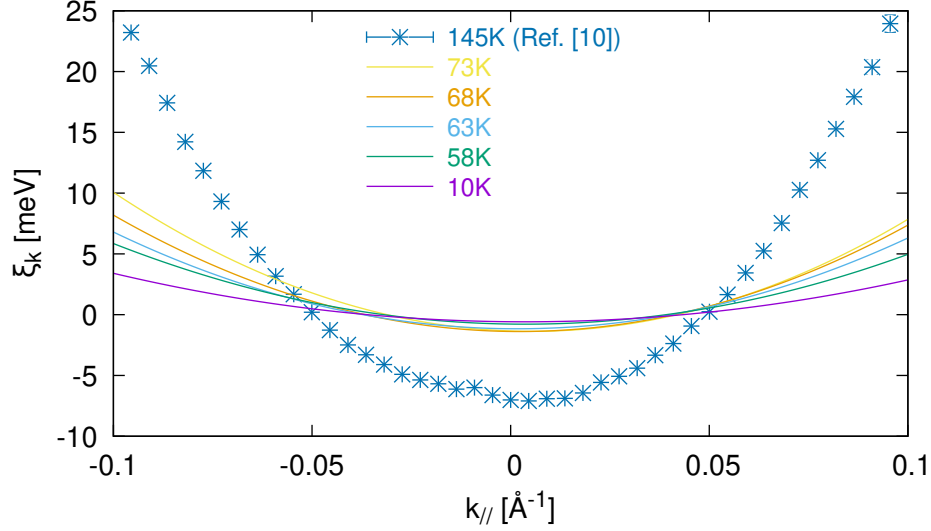


FIG. S2. Normal-state dispersion data at  $T = 145$  K from Ref. [7] and CEH-fitted normal-state dispersion curves at varied temperatures derived from the CEH fits presented in Figs. 3–4.

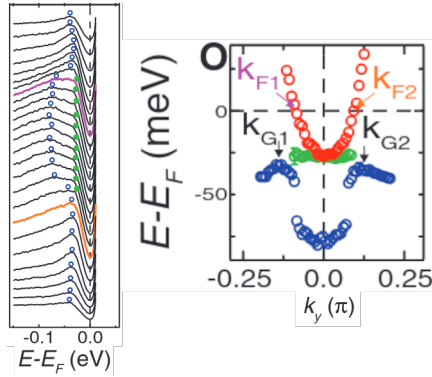


FIG. S3. Quasiparticle band dispersions along the antinodal cut at 10 K for Bi-2201 [9]. Left: EDC waterfall plot. Right: Energy-momentum dispersion curves. Green circles denote the shoulder feature corresponding to CEH band 2, while blue circles indicate CEH band 1 and its cusp feature. Adapted from Fig. 2 of [9].

TABLE II. CEH fitting parameters for Fig. 5.

T [K]	scaling factor for electron branch	scaling factor for hole branch	$\Delta$ [meV]
26	0.24	0.10	11.5
35	0.26	0.12	10.3
45	0.38	0.23	7.7
55	0.48	0.36	5.5

- 
- 229 [1] J. A. Sobota, Y. He, and Z.-X. Shen, *Rev. Mod. Phys.* **93**, 025006 (2021).  
230 [2] Z.-X. Shen, D. S. Dessau, B. O. Wells, D. M. King, W. E. Spicer, A. J. Arko, D. Marshall,  
231 L. W. Lombardo, A. Kapitulnik, P. Dickinson, S. Doniach, J. DiCarlo, T. Loeser, and C. H.  
232 Park, *Phys. Rev. Lett.* **70**, 1553 (1993).  
233 [3] J. G. Bednorz and K. A. Müller, *Z. Physik B - Condensed Matter* **64**, 189 (1986).  
234 [4] Y. Kamihara, H. Hiramatsu, M. Hirano, R. Kawamura, H. Yanagi, T. Kamiya, and H. Hosono,  
235 *J. Am. Chem. Soc.* **128**, 10012 (2006).  
236 [5] J. Bardeen, L. N. Cooper, and J. R. Schrieffer, *Phys. Rev.* **106**, 162 (1957).  
237 [6] H. Matsui, T. Sato, T. Takahashi, S.-C. Wang, H.-B. Yang, H. Ding, T. Fujii, T. Watanabe,  
238 and A. Matsuda, *Phys. Rev. Lett.* **90**, 217002 (2003).  
239 [7] Y. He, S.-D. Chen, Z.-X. Li, D. Zhao, D. Song, Y. Yoshida, H. Eisaki, T. Wu, X.-H. Chen,  
240 D.-H. Lu, and others, *Phys. Rev. X* **11**, 031068 (2021).  
241 [8] J. J. Lee, F. T. Schmitt, R. G. Moore, S. Johnston, Y.-T. Cui, W. Li, M. Yi, Z. K. Liu,  
242 M. Hashimoto, Y. Zhang, D. H. Lu, T. P. Devereaux, D.-H. Lee, and Z.-X. Shen, *Nature* **515**,  
243 245 (2014).  
244 [9] R.-H. He, M. Hashimoto, H. Karapetyan, J. D. Koralek, J. P. Hinton, J. P. Testaud, V. Nathan,  
245 Y. Yoshida, H. Yao, K. Tanaka, and others, *Science* **331**, 1579 (2011).  
246 [10] M. Hashimoto, R.-H. He, K. Tanaka, J.-P. Testaud, W. Meevasana, R. G. Moore, D. Lu,  
247 H. Yao, Y. Yoshida, H. Eisaki, T. P. Devereaux, Z. Hussain, and Z.-X. Shen, *Nature Phys* **6**,  
248 414 (2010).  
249 [11] M. Hashimoto, I. M. Vishik, R.-H. He, T. P. Devereaux, and Z.-X. Shen, *Nature Phys.* **10**, 483  
250 (2014).  
251 [12] W. Tan, *Journal of Physics and Chemistry of Solids* **193**, 112148 (2024).  
252 [13] W. Tan, *Phys. Lett. B* **797**, 134921 (2019), arXiv:1902.01837.  
253 [14] W. Tan, *Universe* **9**, 180 (2023).  
254 [15] J.-H. Ma, Z.-H. Pan, F. C. Niestemski, M. Neupane, Y.-M. Xu, P. Richard, K. Nakayama,  
255 T. Sato, T. Takahashi, H.-Q. Luo, L. Fang, H.-H. Wen, Z. Wang, H. Ding, and V. Madhavan,  
256 *Phys. Rev. Lett.* **101**, 207002 (2008).  
257 [16] P. Zhang, P. Richard, T. Qian, Y.-M. Xu, X. Dai, and H. Ding, *Rev. Sci. Instrum.* **82**, 043712  
258 (2011).